DESIGN OF AN MOM DIODE-COUPLED FREQUENCY-SELECTIVE SURFACE

Edward C. Kinzel,[1] Robert L. Brown,[2] James C. Ginn,[3] Brian A. Lail,[4] Brian A. Slovick,[2] and Glenn D. Boreman[1]
[1] Department of Physics and Optical Sciences, University of North Carolina at Charlotte, 9201 University City Blvd., Charlotte, NC 28223; Corresponding author: gboreman@uncc.edu
[2] CREOL, The College of Optics & Photonics, University of Central Florida, 4000 Central Florida Blvd., Orlando, FL 32816
[3] Plasmonics Inc., 12565 Research Pkwy, Suite 300, Orlando, FL 32826
[4] Electrical and Computer Engineering, Florida Institute of Technology, 150 W. University Blvd., Melbourne, FL 32901

Received 4 July 2012

ABSTRACT: *This article presents the design of a slot-antenna-based frequency selective surface coupled with metal-oxide-metal diodes integrated into the structure. This design takes advantage of a single self-aligned patterning step using shadow evaporation. The structure is optimized at 10.6 μm to have less than 2% reflection with 70% of the incident energy dissipated into the oxide layer. Initial experimental results conducted with e-beam lithography are presented. The fabricated structure is shown to produce a polarization sensitive unbiased DC current. This design will be useful for both infrared sensing and imaging as well as direct conversion of thermal energy.* © 2012 Wiley Periodicals, Inc. Microwave Opt Technol Lett 54:489–493, 2013; View this article online at wileyonlinelibrary.com. DOI 10.1002/mop.27363

Key words: *frequency selective surface; metal-oxide-metal diode; shadow evaporation; infrared; rectenna*

1. INTRODUCTION

Antenna coupled metal-oxide-metal (MOM) diodes have generated significant interest for use in uncooled infrared sensing [1–3] as well as direct energy conversion for solar/thermal harvesting [4]. MOM diodes have been studied at THz and infrared frequencies since the late 1960s [5]. They are attractive for rectification and frequency mixing because of their very fast response times [4] and compatibility with standard CMOS processing [1]. Modern nanofabrication techniques have facilitated their implementation with high-frequency antennas to produce working devices at infrared and optical wavelengths [6].

At radio frequencies, rectennas have achieved up to 90% power transfer efficiency [7]. However, there are obstacles to realizing this performance at infrared/optical wavelengths. One of the most significant is the economic fabrication of nanoscale structures. These feature sizes are dictated by the wavelength of light at optical/infrared frequencies as well as the RC time constant of the diode [5, 6] and the optical properties of metals at infrared/optical wavelengths [8]. For example, Bean et al. [2] predicted that a 75 × 75 nm area overlap or smaller would be required for a diode system similar to what is studied this article not to be cutoff at 28.3 THz. These dimensions are possible with e-beam lithography; however, this is not suitable for economic large-scale production required for either focal plane arrays or for energy harvesting applications. Roll-to-roll nanoimprint lithography (R2RNIL) appears to be a way forward for patterning relatively large areas with the feature sizes required for antenna-coupled diodes [9]. The shadow evaporation technique, proposed by Dolan [10] and developed by Bean et al. [1] allows patterning antenna-coupled diodes with a single patterning step. This will be advantageous for use with R2RNIL because it removes the need for nanoscale alignment between layers.

Both sensing and energy harvesting applications require efficiently capturing radiation from an area larger than that of a single antenna ($\lambda^2/4\pi$ for the lossless isotropic case). This requires the efficient integration of multiple antennas and can be accomplished two ways. Several antennas can be connected to a single diode using transmission lines to form a phased array [3], or each antenna can be connected to its own transducer, which are in turn connected at DC [0]. Ohmic losses and field penetration are much greater in metals at optical and infrared wavelengths than at DC. For example, Mandviwala et al. [0] found the $1/e$ propagation length for standard RF style waveguides to be less than 14 μm at $\lambda_0 = 10.6$ μm. This suggests that it is more efficient to rectify the energy as close to the antenna as possible.

A frequency selective surface (FSS) consists of a periodically arranged array of mutually coupled resonant metallic antenna elements. FSS allows a surface's transmittance, reflectance, and absorptance to be engineered as a function of wavelength, polarization, and angle of incidence. The behavior of the FSS is a function of the geometry of the resonant elements, the array spacing, and the materials making up the elements and the dielectric surface. Similar to rectennas, FSSs were originally developed at microwave frequencies [0], but have been scaled to infrared [0] as well as optical wavelengths. When matched to the incident radiation, they have been demonstrated capable of almost unity absorptance, corresponding to near unity emittance from Kirchhoff's law [0]. In this case, the infrared frequency currents are largely dissipated in the metallic elements of the structure.

This article presents the design, fabrication, and testing of a slot-antenna-based FSS with integrated MOM diodes. It has several advantages for both sensing and energy harvesting. The slot-based design makes use of shadow evaporation for a single patterning step which makes the design scalable to higher volume fabrication. We optimize the structure for polarized radiation at 10.6 μm by impedance matching the FSS to the diode and the entire structure to free space. This wavelength was selected for testing with a CO_2 laser and is near the peak thermal emission from objects at room temperature; however, the design could easily be scaled to shorter wavelengths for energy harvesting. Under linear polarized illumination, the FSS has near-unity absorptance with up to 70% of the power dissipated in the oxide layer. This corresponds to the maximum voltage across the diode which is rectified to produce a DC current. For energy harvesting applications, the FSS can be pared with a second emitting FSS that only radiates the correct polarization and at the optimal wavelength [0, 0]. The article presents the design of the diode-coupled FSS. It is studied and optimized numerically. We then present initial fabrication results which demonstrate the viability of the design. Finally, we discus these results and present suggestions for future work.

2. DESIGN AND SIMULATION

Figure 1(a) shows the geometry of the diode-coupled FSS. Each unit cell is 3.75 × 3.50 μm^2. The FSS consists of a densely packed slot-antenna array separated from an optically thick aluminum ground plane by a 1.6 μm thick benzocyclobutene (BCB) standoff. At the center of each unit cell in the array. The slot antenna is defined in a metal plane that is divided in such way that the diodes are isolated at DC. The thickness of the aluminum and platinum layers are 30 and 25 nm, respectively. The oxide is 1 nm thick and only modeled in the diode gap, following the approach of Ref. 3, and shown in the inset of Figure 1. Simulations show that the high-frequency electromagnetic performance of the FSS is not affected by including the thin oxide

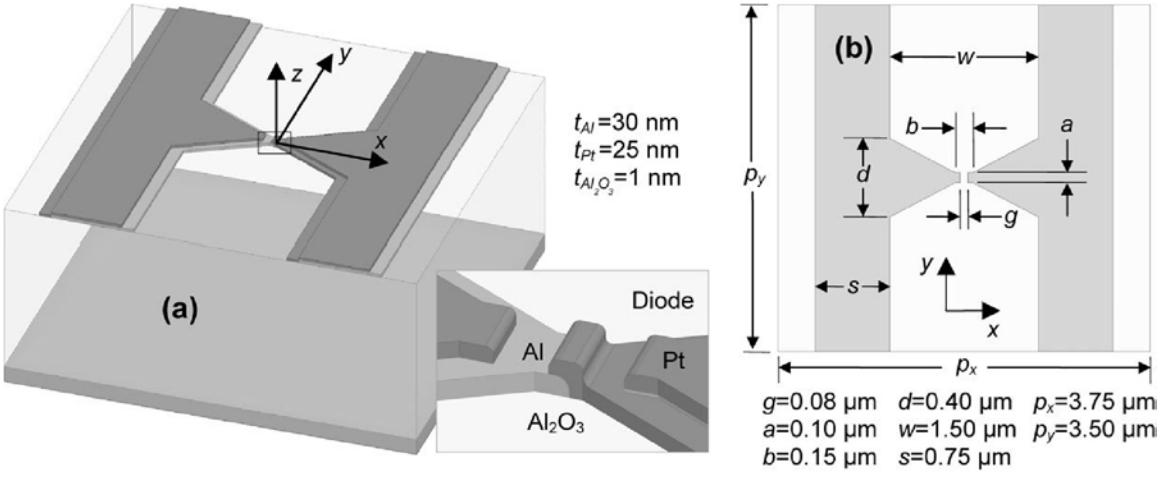

Figure 1 (a) Unit cell geometry and (b) e-beam lithography layout used for defining pattern

layer in other regions and neglecting it simplifies the model, improving the speed during optimization of the structure. Figure 1(b) shows the dimensions of the e-beam lithography pattern used to define the antenna/diode structure.

The unit cell in Figure 1 can be assembled to form a working device, an example of which is shown in Figure 2. Each slot antenna/diode is connected in parallel to bond pads. The net current flow at DC is from the aluminum side of the diode to the platinum. Because the aluminum contact is almost completely covered by platinum it is difficult to probe directly. A gold contact can be deposited prior to patterning the slot antenna/diodes. Gold is attractive because it will not oxidize during the subsequent processing/patterning of the diodes. Because the contact is relatively large, it does not require patterning with e-beam lithography or precise alignment to the finely patterned structure. The feed structure does not capture a significant amount of incident light itself, however making lead lines too small will increase the surface's DC resistance. This produces a tradeoff between the DC and high-frequency performance.

The diode-coupled FSS was modeled as an infinite array and excited with a Floquet port in HFSS (ANSYS Inc.) The geometry of the FSS (w, s, d, p_x, and p_y) was optimized to provide minimal reflection under normally incident 28.3 THz ($\lambda_0 = 10.6$ μm) illumination while maximizing the fraction of power dissipated in the diode oxide. Frequency dependent material properties for Al, Pt, BCB, and Al_2O_3 were obtained from spectrographic ellipsometry (IR-VASE, J.A. Woollam). The native AlO_x oxide is modeled using the properties of Al_2O_3 which has a broad phonon resonance at $\sim$ 12 μm. At $\lambda_0 = 10.6$ μm, the measured permittivity of Al_2O_3 are $\varepsilon' + j\varepsilon'' = -0.41 + j0.11$. Also of note are absorption peaks in BCB centered at 9.5 and 12 μm, however, at $\lambda_0 = 10.6$ μm its properties are $\varepsilon' + j\varepsilon'' = 2.43 + j0.07$. In the structure, the incident field couples to the slot-antenna resonance which induces current through the diode. This resonance can be tuned by adjusting the feature sizes and the standoff. Figure 3 shows the fields in the unit cell when it is exposed to $\lambda_0 = 10.6$ μm x-polarized radiation. The simulation predicts that the electric field is concentrated 2000× across the diode.

Figure 4 shows the simulated reflectance of the FSS for x- and y-polarizations. At the design wavelength, the reflectance is

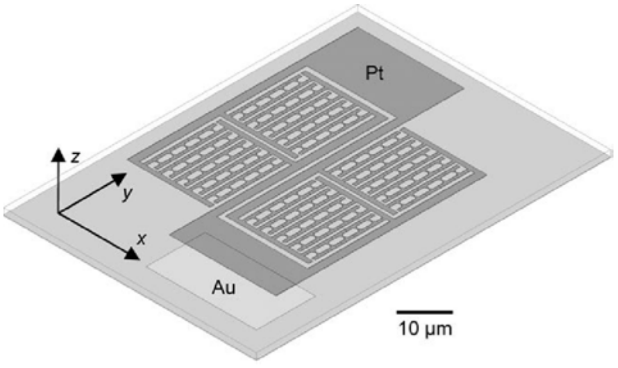

Figure 2 Example device assembled from 100 diode-coupled FSS unit cells in parallel

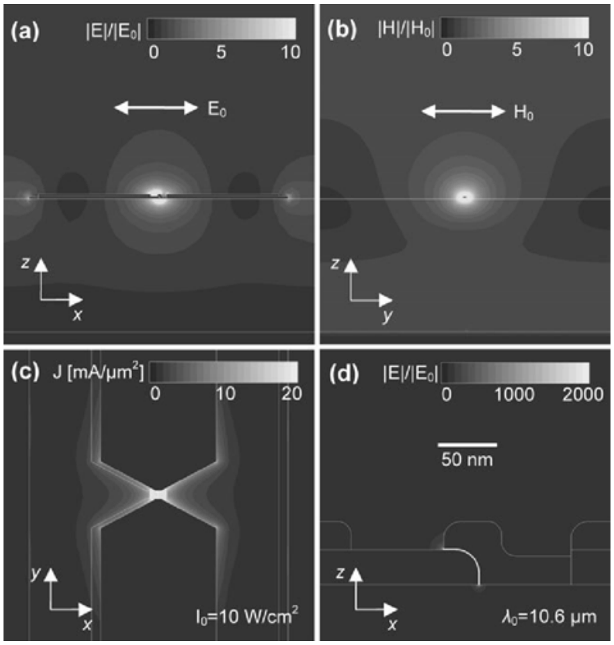

Figure 3 Electromagnetic resonance inducing high-frequency current through diode under y-polarized 10.6 μm normal illumination. (a) E-plane, (b) H-plane, (c) current density on xy plane, and (d) close up of E-field on diode

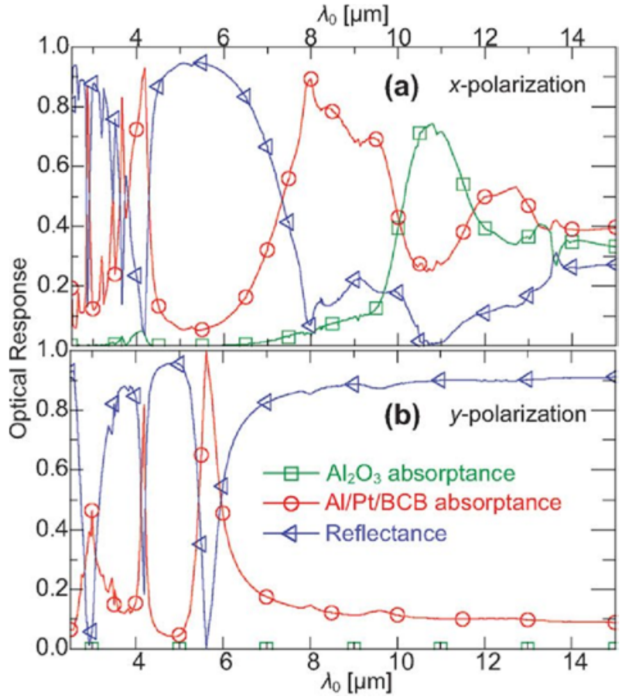

Figure 4 HFSS simulation of FSS response under illumination with (a) *x*-polarized and (b) *y*-polarized lights. [Color figure can be viewed in the online issue, which is available at wileyonlinelibrary.com]

less than 2% for *x*-polarized light and 90% for *y*-polarized illumination. Because of the groundplane, there is no transmission through the structure. More than 70% of the power is dissipated in the oxide due to the extreme field concentration. This shows that the collective structure is well matched to free-space while within the unit cell there is good slot/diode impedance matching. Off-resonance there is less of a match to the oxide and power is instead dissipated in the BCB and metal components of the structure. Figure 5 shows voltage across the diode.

Slovick et al. [3] showed that the power dissipated in the oxide is proportionate to signal (short circuit current) generated by the diode. This is because power dissipated in the oxide scales with the voltage across the diode which determines the rectified current. The first nonzero term in a power series expansion of the rectified current is [3]

$$I_r = \frac{1}{4}\frac{d^2I}{dV^2}\bigg|_{V=V_b} V_0^2 \tag{1}$$

where V_b is the bias voltage and V_0 is the voltage across the diode. The voltage across the diode is evaluated numerically using a line integral of the electric field and plotted in Figure 4 for an incident intensity of 10 W/cm^2. Because of the aspect ratio of the diode, this is close to constant over its area. This differs slightly from the power dissipation due to frequency dependent conductivity of the oxide. It is important to note that this model of the FSS is limited to electromagnetic analysis. Therefore, it is fundamentally linear and does not account for the tunneling effects in the diode.

3. FABRICATION AND MEASUREMENT

The FSS and electrical lead geometry were patterned on top of a 1.6 μm thick BCB standoff above an optically thick aluminum ground plane using the pattern as shown in Figure 1(b). E-beam lithography was used to pattern a bi-layer poly(methyl methacrylate) (PMMA)/MMA resist stack. The underlying MMA is more sensitive to the exposing electron beam than the PMMA which results in a undercut profile after development using MIBK:IPA (1:3). Following development the sample is placed in an O_2 plasma barrel etcher to remove any undesired resist. Proper selection of the pattern geometry and electron beam dosage results in an air-bridge of PMMA in the gap of the antenna. E-beam evaporation is used to deposit Al with the sample rotated a small angle from the normal. The sample is then exposed in situ to 50 mTorr partial pressure O_2 for 30 min which allows a 10–20 Å native oxide layer to form over the exposed Al surface. Following the oxidation step, Pt is deposited at an opposing angle to the first deposition. Provided that there is sufficient undercutting in the MMA, the offset is determined by the deposition angle. The thickness of the oxidation is critical to the process and was studied in detail by Bean et al. in Ref. 2.

Figure 6 shows SEM images of the fabricated device. The globs of material in Figure 6(a) are silver paste used to connect the read-out circuitry to the bond-pad. The experimental device did not use the gold contacts as shown in Figure 2 so must be probed through the platinum. This assumes that there are at least some pinholes in the oxide connecting the platinum layer to the aluminum layer. Because of the large area of the feed structure relative to diode, there is a greater chance that the pinholes will occur outside the active diode region. Figures 8(b) and 8(c) show closer images of the same diode-coupled FSS structure. At least some of the diodes did not completely lift out and contribute to the shorting out of the device. The figures show that there is nontrivial surface roughness in the FSS. This is not a factor electromagnetically, however, within the diode region it contributes to a greater chance of pinholes.

The large number of diode-coupled FSS elements were patterned to provide a sufficient area for FTIR measurements. Figure 7 shows experimental reflectance spectra for the device in Figure 6 collected using a Perkin Elmer micro-FTIR spectrometer. There is qualitative agreement between the experimental and simulated spectra. At the design wavelength, the measurement shows a reflectance of 5% and 80% under *x*- and *y*-polarizations, respectively. The discrepancy between measured and modeled reflectance can be attributed to some of the light being reflected specularly from the feed structure as well as errors in modeling the native oxide's optical properties and exact diode geometry.

Figure 8 shows the DC parameters for the device. The fabricated device behaves as if it was a 125 Ω resistor with limited nonlinearity (8.95 μA/V^2 at 0 bias). This is much less resistance

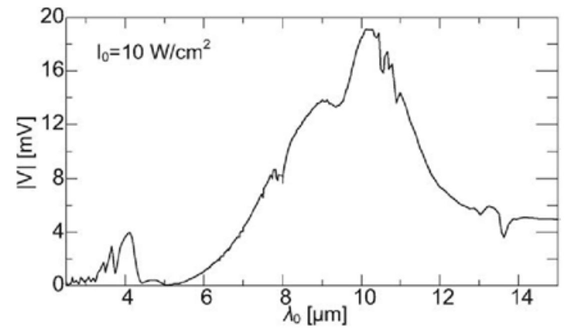

Figure 5 HFSS simulation of voltage across the diode for *x*-polarized light

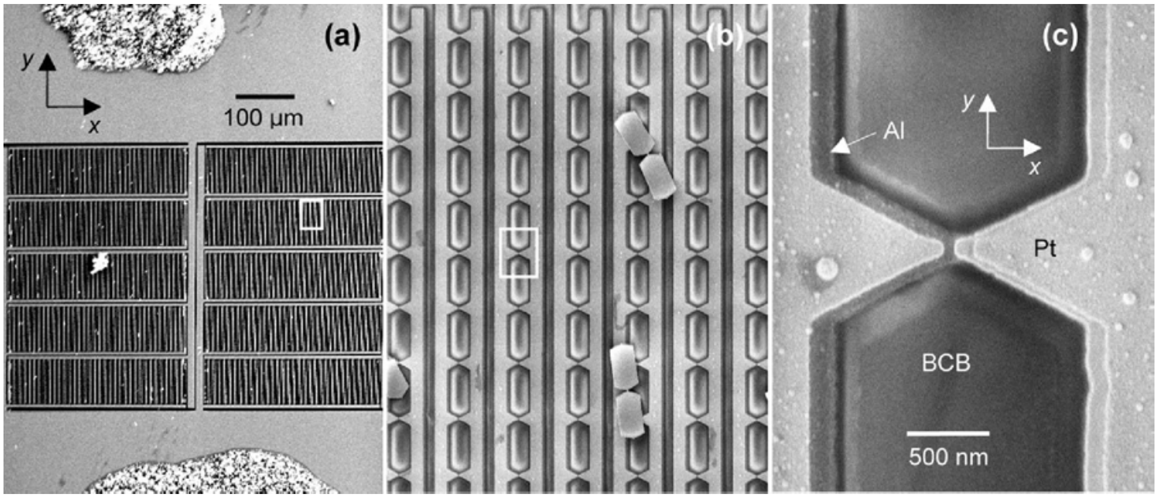

Figure 6 SEM images of fabricated MOM diode-coupled FSS. (a) Image of entire array consisting of 16,800 diode-coupled elements is less than 0.325 mm^2, (b) closer image of the array showing several pieces of metal coated photoresist that became attached to the sample after lift-off, and (c) diode of working device

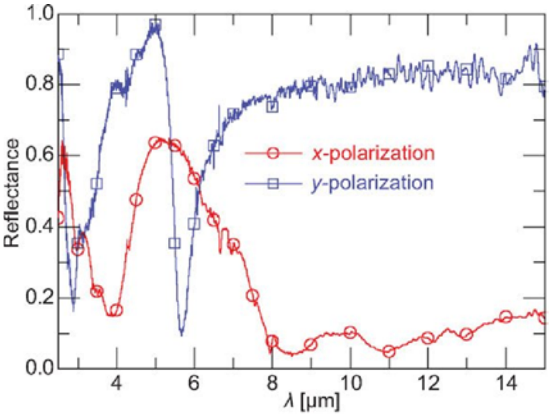

Figure 7 FTIR measured reflectance. [Color figure can be viewed in the online issue, which is available at wileyonlinelibrary.com]

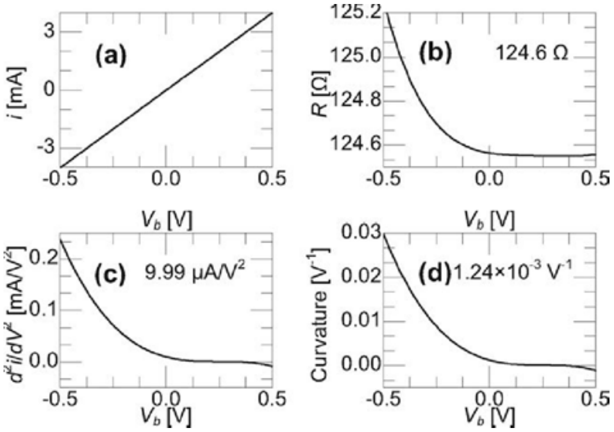

Figure 8 MOM diode-coupled FSS DC response. (a) measured *iv* curve, (b) resistance, (c) nonlinearity, and (d) curvature

(220 kΩ in Ref. 2) as well as lower nonlinearity than other fabricated devices using similar diode dimensions reported in literature (three orders of magnitude lower curvature than [0]). We attribute this to at least some of the diodes being shorted out.

Despite fabrication irregularities, the device does still show some nonlinearity at zero bias. Figure 9 shows the short-circuit response of the device when it is exposed to a polarized CO_2 laser beam. The intensity of the incident beam was ~ 10 W/cm^2. This beam was chopped and the device shown in Figure 8 was connected to a lock-in amplifier. Part of the incident beam was split off and the output of the lock-in amplifier is normalized to the incident beam power. During the experiment, the polarization of the incident beam is rotated with a half-wave plate. The figure shows the polarization dependence of the response indicating that the device is functioning despite some unit cells being shorted out.

The true diode impedance will be a function of the magnitude of the voltage the structure generates across it. That is, the tunneling current will generate an additional resistive component which may effect the matching between the diode, the FSS, and free space. The true diode impedance at the operational frequency is very challenging to measure experimentally. This structure can provide the ability to indirectly infer the impedance from the reflectance spectra. Although it is not explored in

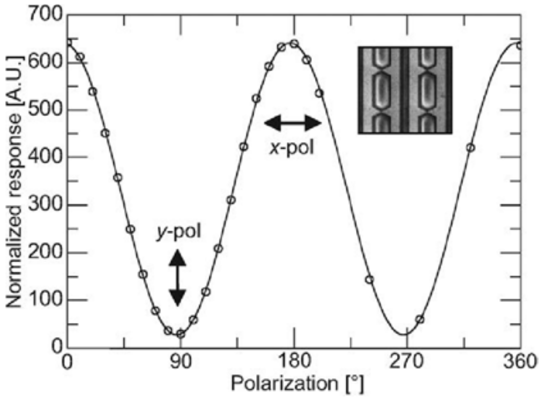

Figure 9 Short circuit response showing polarization dependence

this article, incorporating the slot antennas as an inductive element changes the RC diode system to and RLC system which will affect the cutoff of the diode. This makes the structure resonant at a given frequency as opposed to cutoff at high frequencies and may relieve some of the size constraints on the diode.

4. CONCLUSION

We have designed a diode-coupled FSS. The fabrication process still requires refinement; however, agreement between simulation and initial results is promising and demonstrates that an FSS can be well matched to diodes and to free space. This design was developed for fabrication using self-aligned shadow evaporation. The device was able to resolve the polarization of an incident laser beam. The device has potential for thermal imaging and can be scaled to shorter wavelengths for energy harvesting. The ability to achieve high-field concentrations in a well-confined volume may be useful to other sensing applications. General process engineering improvements to avoid shorting out the diodes should be studied in addition to using a gold contact to directly probe the aluminum side of the diode. Different combination of metal/native oxide/metal systems should also be investigated.

REFERENCES

1. J.A. Bean, B. Tiwari, G.H. Bernstein, P. Fay, and W. Porod, Thermal infrared detection using dipole antenna-coupled metal-oxide-metal diodes, J Vac Sci Technol B 27 (2009), 11–14.
2. J.A. Bean, A. Weeks, and G.D. Boreman, Performance optimization of antenna-coupled Al/AlOx/Pt tunnel diode infrared detectors, IEEE J Quantum Electron 47 (2011), 126–135.
3. B.A. Slovick, J.A. Bean, P.M. Krenz, and G.D. Boreman, Directional control of infrared antenna-coupled tunnel diodes, Opt Exp 18 (2010), 20960–20967.
4. S. Grover and G. Moddel, Applicability of metal/insulator/metal (MIM) diodes to solar rectennas, IEEE J Photovoltaics 1 (2011), 78–82.
5. A. Sanchez, C.F. Davis, Jr., K.C. Liu, and A. Javan, The MOM tunneling diode: Theoretical estimate of its performance at microwave and infrared frequencies, J Appl Phys 49 (1978), 5270–5276.
6. C. Fumeaux, J. Alda, and G. Boreman, Lithographic antennas at visible frequencies, Opt Lett 24 (1999), 1629–1631.
7. W.C. Brown, Optimization of the efficiency and other properties of the rectenna element, Proceedings of the IEEE-MTT-S International Microwave Symposium, 1976, 142–144.
8. L. Novotny, Effective wavelength scaling for optical antennas, Phys Rev Lett 98 (2007), 266802.
9. S.H. Ahn and L.J. Guo, Large-area roll-to-roll and roll-to-plate nanoimprint lithography: A step toward high-throughput application of continuous nanoimprinting, ACS Nano 3 (2009), 2304–2310.
10. G.J. Dolan, Offset masks for liftoff photoprocessing, Appl Phys Lett 31 (1977), 337–339.
11. F.J. Gonzalez, B. Ilic, J. Alda, and G.D. Boreman, Antenna-coupled infrared detectors for imaging applications, IEEE J Sel Top Quantum Electron 11 (2005), 117–120.
12. T.A. Mandviwala, B.A. Lail, and G.D. Boreman, Characterization of microstrip transmission lines at IR frequencies—Modeling fabrication and measurement, Microwave Opt Technol Lett 50 (2008), 1232–1237.
13. B.A. Munk, Frequency selective surfaces, theory and design, Wiley, New York, 2000.
14. C.M. Rhoads, E.K. Damon, and B.A. Munk, Mid-infrared filters using conducting elements, Appl Opt 21 (1982), 2814–2816.
15. X. Liu, T. Tyler, T. Starr, A.F. Starr, N.M. Jokerst, and W.J. Padilla, Taming the blackbody with infrared metamaterials as selective thermal emitters, Phys Rev Lett 107 (2011), 045901.
16. J. Ginn, D. Shelton, P. Krenz, B. Lail, and G. Boreman, Polarized infrared emission using frequency selective surfaces, Opt Exp 18 (2010), 4557–4563.
17. P. Esfandiari, G. Bernstein, P. Fay, W. Porod, B. Rakos, A. Zarandy, B. Berland, L. Boloni, G. Borman, B. Lail, B. Monacelli, and A. Weeks, Tunable antenna-coupled metal-oxide-metal (MOM) uncooled IR detector, Proc SPIE 5783 (2005), 470–482.

DESIGN, MEASUREMENT, AND CHARACTERIZATION OF DUAL-BAND LEFT-HANDED METAMATERIALS WITH COMBINED ELEMENTS

Li Min-Hua,[1] Yang He-Lin,[1] Lin Hai,[1] and Xiao Bo-Xun[2]
[1] College of Physical Science and Technology, Central China Normal University, Wuhan 430079, China; Corresponding author: emyang@mail.ccnu.edu.cn
[2] Engineering Geophysical Research Center, Yangtze University, Jingzhou 434023, China

Received 4 July 2012

ABSTRACT: *We report on a new kind of planar left-handed metamaterial with both simulations and experiments in this article. Dual electric and magnetic resonance frequency bands are experimentally realized by introducing two different metallic elements in one unit cell, which offers a convenient approach in building dual-band or multiband negative-index metamaterials. The effective electromagnetic parameters obtained from the measured S-parameters indicate that negative refractive indexes are verified near 8.5 and 12 GHz with both negative permittivity and negative permeability. Field and current distribution at the dual resonances are also examined. At last, we calculated the radiated power of the magnetic dipole moments along y-axis. The idea can help us to fabricate dual-band or multiband metamaterial absorbers, filters, and antennas.* © 2012 Wiley Periodicals, Inc. Microwave Opt Technol Lett 54:493–497, 2013; View this article online at wileyonlinelibrary.com. DOI 10.1002/mop.27399

Key words: *Metamaterial; left-handed material; negative refraction index; magnetic resonance*

1. INTRODUCTION

Left-handed matamaterials [1, 2] (LHMs) are artificial composite structures that exhibit negative permittivity and permeability. Much of the fascination arises from the unique electromagnetic properties such as reversal of Doppler, enhancement of evanescent wave, subwavelength resolution imaging, and so on. It behaves as a homogeneous material when the lattice constant of the structure and the parameters of the unit cell are small in comparison with the wavelength of interest. Thin conducting wires are commonly used as medium with negative permittivity [3]. Negative electrical response suggests that the wire medium is characterized by a low frequency stop band from zero frequency to the cutoff frequency which is often referred to as plasma frequency (ω_p). Negative magnetic response can be achieved from split-ring resonators proposed by Pendry [4–7]. Experimental investigation of LHMs is done by constructing a composite metamaterial consisting of two components that have $\varepsilon(\omega) < 0$ and $\mu(\omega) < 0$ simultaneously over a certain frequency range. Over this frequency range, a pass band appears in the transmission spectra [8, 9], which is also called LHM-behavior pass band. The index of refraction is less than zero, therefore the phase velocity is orientated the opposite direction of energy flow. This was later followed by numerous analytical formulations [10–12] of the LH medium.

Multiband LHMs were demonstrated [13, 14] by alternatively stacking arrays of LH unit cells with different geometrical